Toward the production of renewable diesel over robust Ni nanoclusters highly dispersed on a two-dimensional zeolite

Hao Pang[1,2], Guoju Yang [1], Lin Li[3] and Jihong Yu [1,2]

Abstract

Deoxygenation of bioderived lipids into renewable transportation fuels is a promising route to decreasing the dependence on fossil sources. Ni-based catalysts are high performing and cost-effective in deoxygenation reactions but suffer from severe sintering and aggregation. Herein, a ligand-chelating impregnation method was used to prepare highly dispersed Ni nanoclusters on a two-dimensional (2D) ITQ-2 zeolite. Comprehensive characterization was utilized to monitor the changes in the organometallic precursors during activation and to investigate their impact on the dispersion of the Ni nanoclusters on the ITQ-2 zeolite. The high external surface area and abundant surface defects of the 2D support enhanced the dispersion and immobilization of the Ni nanoclusters and outperformed conventional zeolites. The protection of the Ni^{2+} cations by the organic ligand suppressed the aggregation of Ni species during the activation processes, thereby leading to the formation of uniformly distributed Ni nanoclusters on the ITQ-2 zeolite. Due to the highly dispersed Ni nanoclusters and immobilization on the 2D zeolite, the Ni/ITQ-2-co material prepared by the ligand-chelating impregnation approach showed outstanding activity and stability for conversions of stearic acid or palm oil to diesel range alkanes. This work provides a rational design and precise modulation of metal-based catalysts for the production of renewable diesel.

Introduction

The dwindling stores of fossil fuels and the escalating environmental problems arising from their overuse have made it urgent to develop alternative sustainable energy sources. Biomass-derived triglycerides (TGs) are promising candidates and have been extensively utilized to produce liquid fuels due to their abundances, renewability, eco-friendliness, and high energy densities[1–3]. The transesterification reaction between a TG and an alcohol over an acid or base catalyst has been commercialized around the world to produce fatty acid alkyl esters (FAMEs), which are viewed as first-generation biodiesel[4].

Despite the environmental benefits, high flash point, and excellent lubricity, there are drawbacks of FAMEs that severely limit extensive utilization, such as low oxidative stability, weak cold flow properties, and high residual oxygen content[5].

To overcome the disadvantages of FAMEs, catalytic deoxygenation processes (hydrodeoxygenation, decarbonylation, and decarboxylation) have been developed to produce diesel-range alkanes by removing oxygen from the free fatty acids (FFAs) or TGs[6–8]. Sulfided metal catalysts, such as sulfided nickel and molybdenum[9,10], show high catalytic performance in the conversion of TGs to diesel-range alkanes. However, sulfur leaching from catalysts can cause catalyst deactivation and diesel product contamination.

Various supported metal catalysts have shown significant potential for use in the deoxygenation reactions of TGs or FFAs to produce diesel-range alkanes, such as Ru[11], Pt[12], Pd[13], Ni[14], Co[15], Cu[14], etc. Support materials

Correspondence: Guoju Yang (yanggj@jlu.edu.cn) or
Jihong Yu (jihong@jlu.edu.cn)
[1]State Key Laboratory of Inorganic Synthesis and Preparative Chemistry, College of Chemistry, Jilin University, 2699 Qianjin Street, Changchun 130012, P. R. China
[2]International Center of Future Science, Jilin University, 2699 Qianjin Street, Changchun 130012, P. R. China
Full list of author information is available at the end of the article

enhance the distributions and stabilities of the metal sites and promote the catalytic capabilities of metal-based catalysts[16].

Zeolites with orderly distributed micropores, unique shape selectivities, high stabilities, and tunable acidic/basic sites are promising supports for metals[17–21]. Zeolite-supported metal catalysts (metal/zeolite) have gained tremendous research interest for use in deoxygenation reactions and other biomass upgrading processes[22–24]. Among these catalysts, Ni/zeolite catalysts are highly promising, owing to their sufficient activity and low costs[7]. Impregnation, ion exchange, and deposition-precipitation are the most commonly used approaches for loading Ni onto zeolite supports, but their disadvantages, such as low dispersion, limited concentration of exchangeable sites, and complex operations, must be overcome[25,26]. Zhao and her coauthors prepared core-shell structured Ni/Beta and hierarchical Ni/HUSY zeolites using a two-step dissolution–recrystallization process and a post-treatment strategy, respectively[6,7]. Both of them exhibited high catalytic activity in the deoxygenation reactions of TGs or FFAs. However, high Ni loadings (≥ 10 wt.%) on the zeolites are needed for the deoxygenation reactions, and the abundant Ni clusters are prone to sintering and aggregation during the activation and reaction processes. Recently, Li et al. prepared ultrasmall Co clusters on H-ZSM-5 zeolite by grafting cobaltocene to the Brønsted acid sites of zeolites[27]. ZSM-5 zeolites with three-dimensional micropores suffer from severe diffusion limitations for bulky molecules, such as TGs and FFAs. Therefore, it is highly desirable to prepare robust Ni/zeolites that integrate stable and highly dispersed metal clusters with excellent mass transfer efficiencies on the zeolites for deoxygenation reactions of TGs and other bulky compounds.

In this work, highly dispersed Ni nanoclusters were distributed on 2D ITQ-2 zeolite, which possesses an open framework structure and high external surface area, and a facile impregnation strategy was used that involves organometallic chemistry and is hereafter referred to as "ligand-chelating impregnation". The cyclic organic amine (1,4,7,10-tetraazacyclododecane, abbreviated as cyclen)-chelated Ni^{2+} cation was used as a precursor. A number of characterization techniques, including electron microscopy, spectroscopic analyses, temperature-programmed hydrogen reduction (H_2-TPR), and thermogravimetry analysis (TG), were used to investigate the effects of the ligand-chelated metal precursors and the microenvironments on the zeolite support providing immobilization and dispersion of the Ni species. The prepared Ni/zeolites were used for deoxygenation of bulky biomass-derived stearic acid (SA) or palm oil to produce diesel-range alkanes, which are regarded as promising renewable transportation fuels. The 2D Ni/ITQ-2-co zeolite prepared by the ligand-chelating impregnation method showed a higher catalytic rate than the Ni/Y analog, with over a 10-fold improvement. In addition, due to immobilization by the 2D zeolite, the Ni/ITQ-2-co catalyst displayed outstanding stability during the deoxygenation reactions. This facile synthetic strategy can be used to prepare other robust metal-based catalysts for complicated biomass conversions.
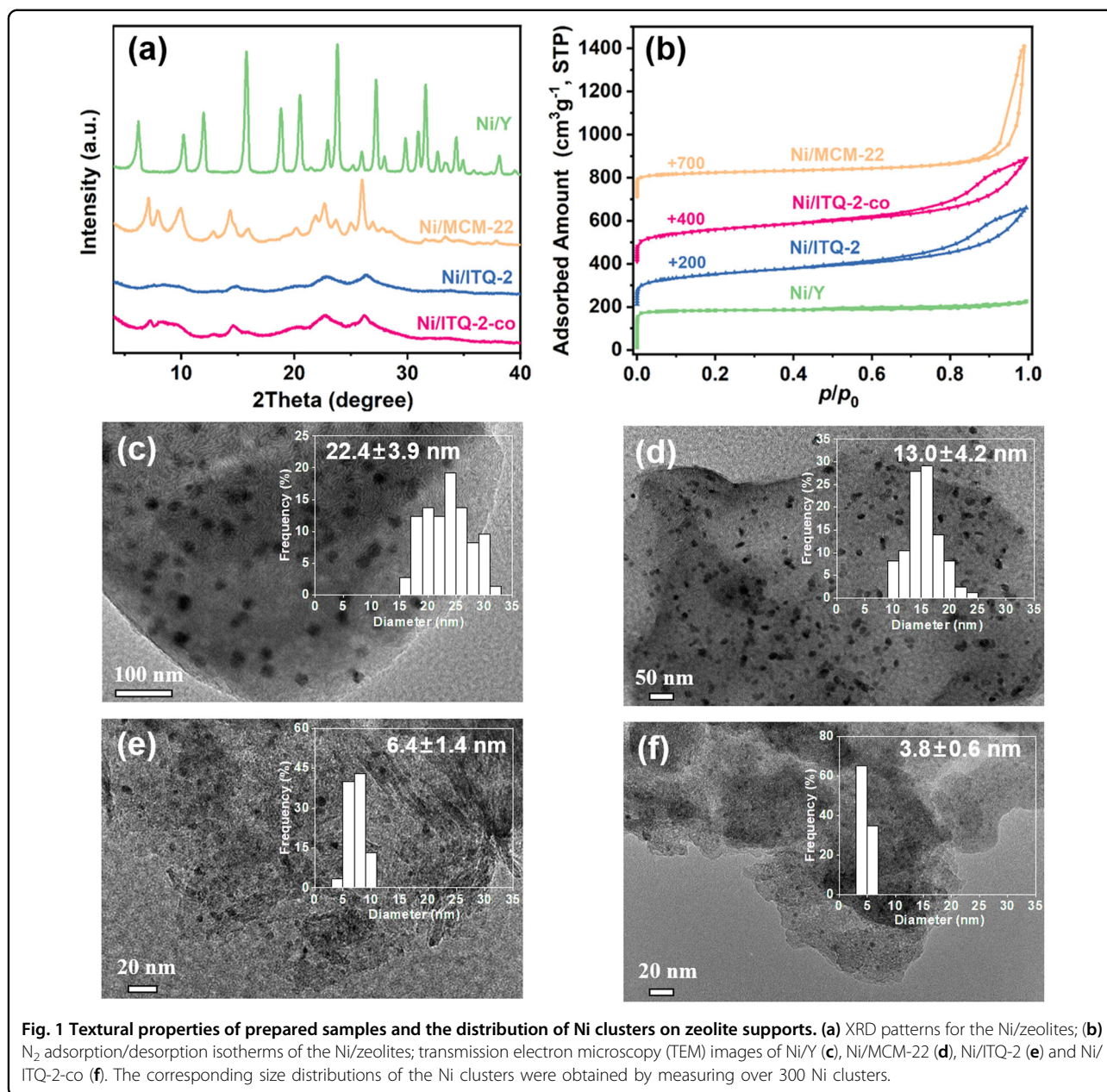
Materials and methods

The zeolite supports (Y, MCM-22, and ITQ-2) were prepared with previously reported methods[28–30]. The Ni species was loaded on the zeolite with a conventional impregnation method and the ligand-chelating impregnation strategy. The materials and chemicals used in this work and the synthetic methods, characterization techniques, and catalytic tests are described in detail in the Supplementary Information.

Results and discussion

Physicochemical properties of the Ni/zeolite materials

The X-ray diffraction (XRD) patterns for the prepared samples are shown in Fig. 1a and Fig. S1. The typical diffraction peaks for Y, MCM-22, and ITQ-2 zeolites are observed in Fig. S1[28,29]. There were no other peaks for amorphous or competing phases appearing in these XRD patterns. The XRD pattern for the Ni/zeolite material is given in Fig. 1a, and the intensities of diffraction peaks for the Ni/zeolites were hardly changed after loading of the Ni species and subsequent activation, indicating that the zeolite framework was preserved.

N_2 adsorption/desorption isotherms and the porosity parameters of the prepared Ni/zeolite materials are shown in Fig. 1b and summarized in Table S1, respectively. Unlike Ni/Y (with a type-I isotherm implying a microporous structure), the Ni/ITQ-2 and Ni/MCM-22 samples displayed type-IV isotherms with a second uptake at a relative pressure (p/p_0) between 0.8 and 1.0, indicating the presence of intercrystalline meso-/macropores in the zeolite support. Ni/Y had the largest total surface area (S_{total}, 604 $m^2 \cdot g^{-1}$) and micropore volume (V_{micro}, 0.26 $cm^3 \cdot g^{-1}$) among the prepared Ni/zeolites. The laminar Ni/MCM-22 sample showed a larger external surface area (S_{ext}, 147 $m^2 \cdot g^{-1}$) than Ni/Y (57 $m^2 \cdot g^{-1}$). 2D Ni/ITQ-2 and Ni/ITQ-2-co displayed large S_{ext} values (431 and 415 $m^2 \cdot g^{-1}$, respectively) owing to the open structure of the 2D zeolite. The pore size distributions of the Ni/zeolite samples are given in Fig. S2. Apparent mesopore distributions were observed for the laminar and 2D Ni/zeolite samples, which could have resulted from aggregation of the interlayer mesopores. Other physicochemical properties of the prepared Ni/zeolites are also compiled in Table S1. An ICP–OES analysis showed comparable Ni loadings (~2.3 wt.%) for the prepared

Fig. 1 Textural properties of prepared samples and the distribution of Ni clusters on zeolite supports. (a) XRD patterns for the Ni/zeolites; **(b)** N$_2$ adsorption/desorption isotherms of the Ni/zeolites; transmission electron microscopy (TEM) images of Ni/Y **(c)**, Ni/MCM-22 **(d)**, Ni/ITQ-2 **(e)** and Ni/ITQ-2-co **(f)**. The corresponding size distributions of the Ni clusters were obtained by measuring over 300 Ni clusters.

samples. The ratio of silicon to aluminum (Si/Al) was 16.7 for the laminar sample and 20.0 for the 2D Ni/zeolites.

The morphologies of the zeolite supports were determined with scanning electron microscopy (SEM). As shown in Fig. S3, the Y zeolite showed a pyramid-like morphology with an average particle size of ~1 μm. Curved and soft stacked nanosheets were observed for the MCM-22 (Fig. S3b) and ITQ-2 (Fig. S3c) samples. After loading of the Ni clusters, the morphologies of the zeolite supports hardly changed (Fig. S4), indicating that the zeolite supports were stable during the impregnation treatment. The effects of the zeolite morphology and micro/nanostructure on the dispersion of the Ni clusters

was monitored by TEM analysis. As shown in Fig. 1c–f, the average sizes of Ni clusters in the prepared Ni/zeolite samples were approximately 3 to 24 nm, which were much larger than the micropore size of each zeolite, suggesting that the Ni clusters were mainly distributed on the external surfaces of the supports. Significantly, the particle sizes of the Ni clusters varied with the micro/ nanostructure of each zeolite support. The 2D ITQ-2 zeolite with the larger external surface area supported smaller Ni clusters than the 3D and laminar zeolites. The average sizes of the Ni nanoparticles in the catalysts decreased in the order Ni/Y > Ni/MCM-22 > Ni/ITQ-2 > Ni/ITQ-2-co. Compared with the 3D and laminar zeolite
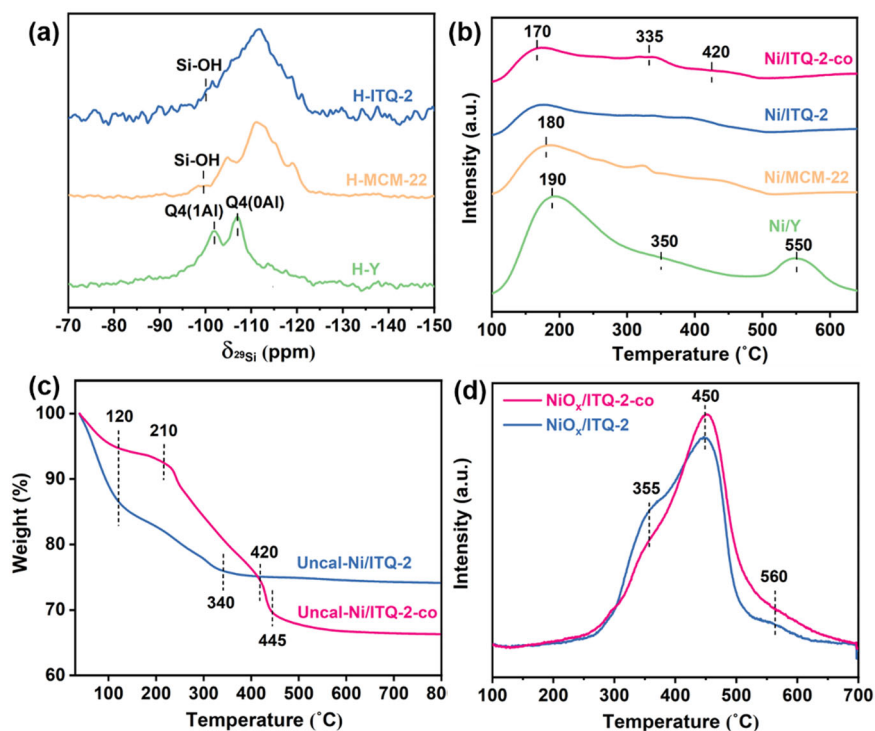
Fig. 2 Framework environment of supports and evolution of Ni species during activation process. a ^{29}Si NMR spectra of the prepared zeolite supports. **b** NH$_3$-TPD profiles of the prepared Ni/zeolite samples; **c** TG analyses of the uncalcined Ni/ITQ-2 and Ni/ITQ-2-co samples; **d** H$_2$-TPR profiles of the NiO$_x$/ITQ-2 and NiO$_x$/ITQ-2-co materials that were calcined before reduction.

supports, the average Ni nanoparticle sizes of Ni/ITQ-2 and Ni/ITQ-2-co were as small as 6.4 ± 1.4 nm and 3.8 ± 0.6 nm, respectively. The small Ni clusters on the 2D ITQ-2 zeolite implied that the larger external surface area favored dispersion of the metal particles. For the same 2D ITQ-2 support, the Ni clusters uniformly immobilized on Ni/ITQ-2-co were smaller than those on Ni/ITQ-2, suggesting that the introduction of an organic ligand to chelate the Ni precursor prior to impregnation played an essential role in immobilizing the metal species and increasing their dispersion during calcination and the subsequent reduction processes.

In addition, energy-dispersive X-ray spectroscopy (STEM-EDS) was used to determine the distributions of the elements in the Ni/ITQ-2 and Ni/ITQ-2-co samples (Fig. S5). The STEM-EDS images showed that the elemental Ni was well distributed on the ITQ-2 support. However, compared with the uniformly distributed Ni clusters on Ni/ITQ-2-co, some of the Ni clusters in Ni/ITQ-2 were obviously agglomerated, which was consistent with the TEM observations.

^{29}Si MAS NMR spectra of the zeolite supports are shown in Fig. 2a. Two strong signals at −102 ppm to −107 ppm appeared in the spectrum of H-Y, which were assigned to Q4(1Al) and Q4(0Al) in the H-Y

zeolite[31]. Moreover, the shoulder peak at −100 ppm indicated the presence of minimal silanol species distributed on the external surface of the H-Y zeolite[32]. For the ITQ-2 and MCM-22 samples, the signals at −105 to −120 ppm corresponded to the Q4 environments, while the Q3 T-sites (Si(OSi)$_3$OH) exhibited peaks at ca. −100 ppm[33,34]. After deconvolution, the populations of the Q3 sites were 18% in ITQ-2 and 8% in MCM-22, signifying that ITQ-2 had more Si-OH defect sites than MCM-22. Furthermore, the influence of Ni introduction into ITQ-2 at the Si-OH sites was studied by Fourier transform infrared spectroscopy (FTIR). As shown in Fig. S6a, introduction of the Ni species into ITQ-2 resulted in decreases in the number of isolated Si−OH sites exhibiting bands that were centered at 3745 cm^{-1}, implying that the defect sites (Si−OH) in ITQ-2 were covered by the Ni species. Therefore, based on the above analyses of the Si-OH sites by ^{29}Si MAS NMR and FTIR, it can be deduced that the abundant isolated Si−OH defects on ITQ-2 are probably effective in immobilizing the Ni species, thereby leading to better dispersion and smaller particle sizes for the Ni clusters compared with those on the MCM-22 and Y zeolite supports. The above results were consistent with the TEM analysis (Fig. 1c−f).
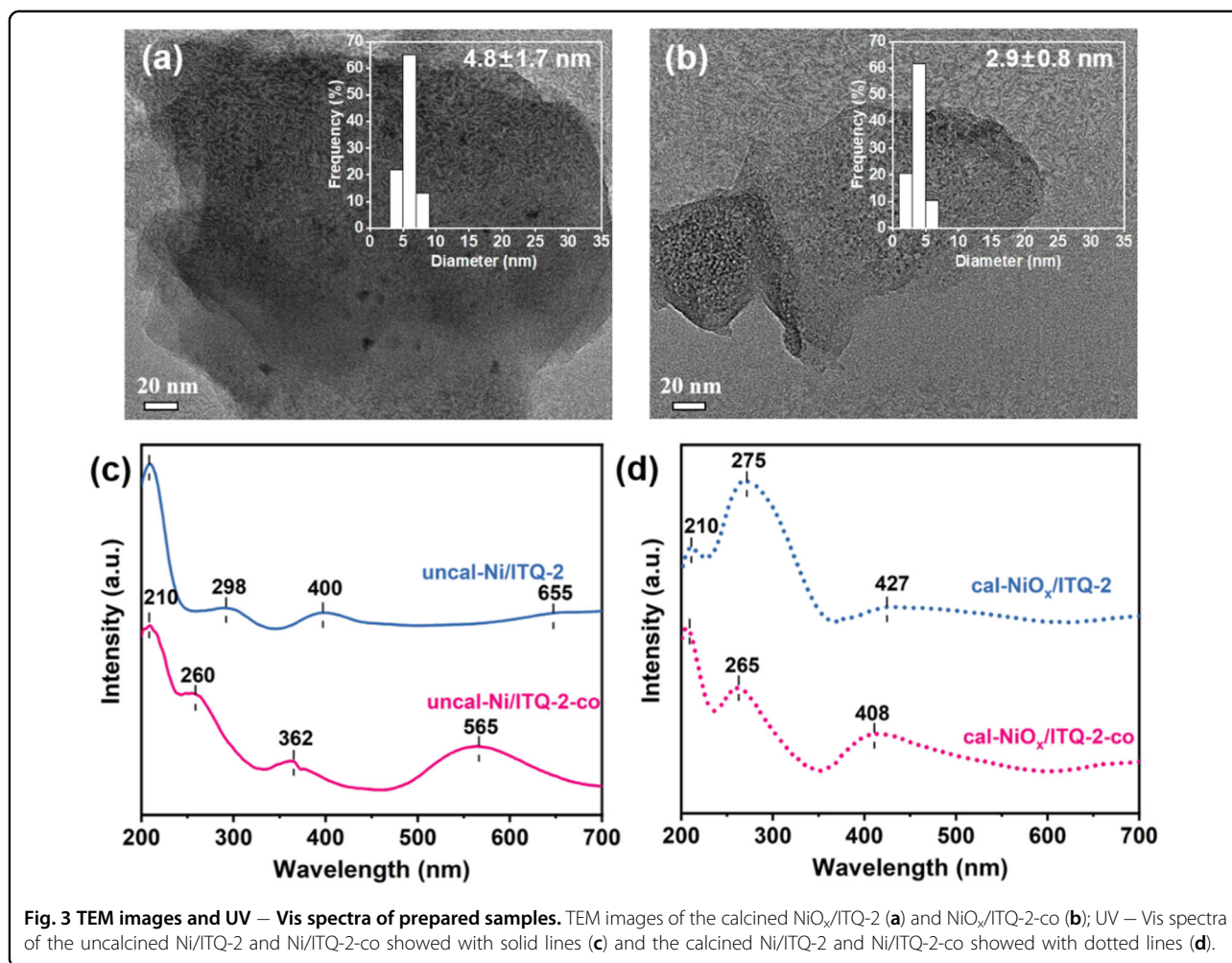
The profiles for temperature-programmed desorption of ammonia (NH$_3$-TPD) from the prepared samples are given in Fig. 2b. An apparent desorption peak at 170–190 °C was observed for all of the samples, and this was ascribed to weakly acidic sites, such as defect sites (Si-OH, etc.)[35]. The desorption peak at 335–350 °C was attributed to the desorption of ammonia from medium acid sites[36]. For the Ni/MCM-22 and Ni/ITQ-2(-co) samples, the desorption peaks at approximately 420 °C corresponded to the desorption of ammonia from strong Brønsted acid sites[37]. The acidity of ITQ-2 was weaker than that of MCM-22, which may be attributed to dealumination occurring during the swelling process[28]. Among the samples, the Ni/Y exhibited the highest acid concentration and strength (at 550 °C) and the lowest Si/Al ratio and a unique framework structure.

TG analyses of the as-synthesized Ni/ITQ-2 and Ni/ITQ-2-co samples (uncalcined) were conducted to investigate the effect of the chelating ligand on the Ni species formed during calcination. The TG results showed that the mass-loss profiles of the uncalcined samples were affected by the presence of the cyclen ligand. As shown in Fig. 2c, in addition to the mass loss seen at 120 °C, which corresponded to water removal from the two samples, stepwise mass losses from 120−450 °C were observed for the Ni/ITQ-2-co samples; this included a gradual loss at 120−210 °C and two sharp losses at 210 and 420 °C, which implied stepwise decomposition of the Ni-cyclen complex on ITQ-2 during calcination. The organic species in Ni/ITQ-2-co was completely removed at 500 °C in flowing air. In comparison, an apparent mass loss at 120−210 °C for Ni/ITQ-2 indicated quick combustion of the nickel nitrate on ITQ-2 zeolite. The TG data for the uncalcined Ni/ITQ-2 and Ni/ITQ-2-co showed that Ni-cyclen was more stable during calcination than the bare Ni cations on the zeolite. Stepwise decomposition of the Ni-cyclen complex could stabilize the Ni species and inhibit rapid aggregation during calcination, thereby improving the dispersion of NiO$_x$ on the ITQ-2 zeolite.

The H$_2$-TPR profiles for the calcined NiO$_x$/ITQ-2 and NiO$_x$/ITQ-2-co are shown in Fig. 2d. A sharp peak at 450 °C and two small peaks centered at 355 °C and 560 °C were identified for these two samples. The low-temperature peak at 355 °C was ascribed to the bulky NiO$_x$ particles distributed on the surface of ITQ-2, which were reduced at low temperatures[38]. NiO$_x$/ITQ-2 exhibited higher profiles at 355 °C than NiO$_x$/ITQ-2-co, indicating that bulkier NiO$_x$ clusters were formed on NiO$_x$/ITQ-2 via aggregation of the Ni species during calcination. The sharp peak at 450 °C corresponded to the highly dispersed NiO$_x$ that was strongly immobilized on the zeolite support, which resulted in the higher reduction temperature[39]. Compared with NiO$_x$/ITQ-2, for which nickel nitrate was used as the precursor, the NiO$_x$/ITQ-2-co prepared by the ligand-chelating impregnation approach exhibited more highly dispersed NiO$_x$ clusters that were strongly immobilized on ITQ-2. These H$_2$-TPR results were confirmed by TEM analyses of the calcined NiO$_x$/ITQ-2 and NiO$_x$/ITQ-2-co samples. As shown in Fig. 3a, b, uniform NiO$_x$ clusters with an average size of 2.9 ± 0.8 nm were more homogeneously distributed throughout the NiO$_x$/ITQ-2-co sample (Fig. 3b), compared with NiO$_x$/ITQ-2 with an average size of 4.8 ± 1.7 nm (Fig. 3a). These support-stabilized NiO$_x$ species suppressed quick agglomeration of the NiO$_x$ species during reduction in H$_2$, thereby efficiently improving the dispersion of the Ni clusters. The reduction peak at 560 °C was assigned to the exchanged Ni^{2+} on the zeolite structure, which required a higher reduction temperature than NiO$_x$[40]. Thus, the reductions for all of the prepared samples were performed at 560 °C.

The nickel species influenced by the organic ligand and the ITQ-2 support were characterized by ultraviolet−visible diffuse reflectance spectroscopy (UV − Vis). The UV − Vis spectra of uncalcined and calcined Ni/ITQ-2 and Ni/ITQ-2-co are shown in Fig. 3c, d. A single band at 210 nm was ascribed to the characteristic charge-transfer transition of the tetracoordinated aluminum in the zeolite framework[41]. When neat Ni(NO$_3$)$_3$ was used as the precursor for impregnation on ITQ-2, UV spectral bands at 298, 400, and 655 nm were detected (Fig. 3c), and these were assigned to the charge-transfer transition of NO$_3^-$ with Ni^{2+} and the d–d transition of [Ni(H$_2$O)$_6$]$^{2+}$ on the zeolites[42,43]. When the ITQ-2 zeolite was impregnated with the cyclen-chelated Ni^{2+} complex, higher energy UV bands were observed compared to the Ni/ITQ-2 sample. As shown in Fig. 3d, three distinct bands were observed at 260, 362, and 565 nm. The band at 260 nm was ascribed to the isolated distorted octahedral Ni^{2+} complexes that were immobilized on the zeolite support[43]. The presence of the isolated Ni^{2+} species suggested that cyclen chelation prevented aggregation of the Ni^{2+} species impregnated on the zeolites. In addition, two bands at 362 and 565 nm corresponded to d–d transitions of the Ni^{2+} complex in Ni/ITQ-2-co. The higher energies of the Ni^{2+} d–d transition bands compared with those for Ni/ITQ-2 were caused by the presence of a strong organic ligand that coordinated the Ni^{2+} cations[42]. In addition, the effect of the interactions between the Ni-cyclen complex and the ITQ-2 support on the distinct coordination environment identified by UV − Vis cannot be neglected. Several spectroscopic studies have demonstrated strong interactions of organometallic complexes and acidic OH groups on the support surface[27,44,45]. The strong interactions of the Ni-cyclen complex with the acidic surface of the ITQ-2 after impregnation enabled uniform distribution of the Ni precursor. Thus, the use of a ligand-chelated Ni complex as the precursor in the impregnation process

Fig. 3 TEM images and UV − Vis spectra of prepared samples. TEM images of the calcined NiO$_x$/ITQ-2 (**a**) and NiO$_x$/ITQ-2-co (**b**); UV − Vis spectra of the uncalcined Ni/ITQ-2 and Ni/ITQ-2-co showed with solid lines (**c**) and the calcined Ni/ITQ-2 and Ni/ITQ-2-co showed with dotted lines (**d**).

improved the molecular interactions with the zeolite support and protected the active Ni species from agglomeration.

The distributions of the organometallic complexes on the zeolites were also confirmed by FTIR analyses. As shown in Fig. S6b, the uncalcined Ni/ITQ-2-co sample prepared by the ligand-chelating impregnation route showed two obvious C-H stretching vibrations at 2944 and 2894 cm^{-1}, which implied the presence of the Ni-cyclen complex on the ITQ-2 support. The FTIR results were consistent with the UV−Vis analyses. These results showed the ligand enabled uniform immobilization of the Ni species on the ITQ-2 zeolite by chelating the Ni cations in the precursor solution.

A band at approximately 265 nm with a shoulder at 408 nm was observed in the UV spectrum of NiO$_x$/ITQ-2-co (Fig. 3d). However, NiO$_x$/ITQ-2 exhibited two bands at 275 and 427 nm. These bands were ascribed to NiO$_x$ species, as reported in the literature[46]. Indeed, shifts of NiO$_x$ bands toward higher wavelengths for NiO$_x$/ITQ-2 indicated the NiO$_x$ particles were larger than those in

NiO$_x$/ITQ-2-co[47], which was consistent with the average NiO$_x$ sizes determined in the TEM analysis (Fig. 3b).

The electronic states of the Ni species in the Ni/ITQ-2 and Ni/ITQ-2-co samples were determined by X-ray photoelectron spectroscopy (XPS), which was used to investigate the interactions between metallic Ni (Ni^0) and the ITQ-2 zeolite. The XPS spectra of Ni/ITQ-2 and Ni/ITQ-2-co are shown in Fig. S7. Deconvolution of the Ni 2p XPS peak resulted in four peaks at ca. 855.4 or 856.5 eV for Ni^0 (2p$_{3/2}$), 862.1 eV for Ni^{2+} (2p$_{3/2}$), 874.5 eV for Ni^0 (2p$_{1/2}$), and 880.8 eV for Ni^{2+} (2p$_{1/2}$)[48]. Compared with the isolated nickel metal, which exhibited a Ni^0 (2p$_{3/2}$) binding energy (BE) of 853 eV, the ITQ-2-supported nickel showed higher BEs (∼856 eV) for Ni^0 (2p$_{3/2}$) due to the electronic influence of the zeolite support[49]. It has been reported that interactions of metal clusters with oxygens in the zeolite framework gave rise to positive charges on the metal surface and higher BEs for the metal nanoclusters[50,51]. As shown in Fig. S7, Ni/ITQ-2 exhibited a main peak at 855.4 eV for Ni^0 (2p$_{3/2}$), while the Ni^0 (2p$_{3/2}$) peak was at 856.5 eV for Ni/ITQ-2-co. The

Scheme 1 The deoxygenation reaction of stearic acid for diesel production.
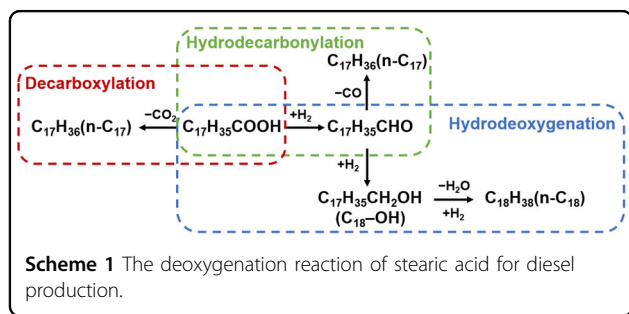
higher BE for Ni^0 in Ni/ITQ-2-co indicated that the Ni nanoclusters loaded by the ligand-chelating impregnation method had stronger interactions with the ITQ-2 support relative to those seen after the conventional impregnation approach[48]. This could have originated from more highly dispersed NiO_x that was strongly stabilized on the ITQ-2 before reduction, as demonstrated by the TG and H_2-TPR analyses provided above. Furthermore, the strongly immobilized Ni nanoparticles on Ni/ITQ-2-co inhibited rapid aggregation during the reaction.

Catalytic performance of the Ni/zeolite catalysts

The deoxygenation reaction of SA was used as a model reaction for conversions of FFAs to diesel-range alkanes. The reaction routes for SA conversion are depicted in Scheme 1. SA could undergo full hydrogenation of the carboxyl group to produce 1-octadecanol, which may be converted to octadecene by acid-catalyzed dehydration. Octadecene is easily hydrogenated at metal sites to yield n-octadecane. In addition, partial hydrogenation of the carboxyl group would produce stearaldehyde, which could also be converted to n-heptadecane through decarbonylation. Alternatively, the SA could also produce heptadecene directly via decarboxylation.

In the present work, the catalytic activities of the prepared 3D and 2D Ni/zeolites were investigated with the deoxygenation of SA (Fig. 4). The normalized reaction rate was calculated with Equation S1 to compare the catalytic activities for all of the Ni/zeolite materials prepared. As shown in Fig. 4a, the normalized rates of the samples increased in the order Ni/Y < Ni/MCM-22 < Ni/ITQ-2 < Ni/ITQ-2-co. The 2D Ni/ITQ-2 catalyst exhibited a remarkably higher conversion rate (90 g_{SA} g_{Ni}^{-1} h^{-1}) compared to those of the laminar Ni/MCM-22 (50 g_{SA} g_{Ni}^{-1} h^{-1}) and 3D Ni/Y (12 g_{SA} g_{Ni}^{-1} h^{-1}) samples. The enhanced activity of Ni/ITQ-2 was attributed to the open structure and more accessible acid sites in 2D ITQ-2, which promoted dehydration and facilitated conversion of the SA. In addition, the abundant defect sites on the ITQ-2 surface aided the dispersion of the Ni clusters on the ITQ-2 support. Thus, the highly dispersed Ni nanoparticles promoted deoxygenation reactions. Compared with Ni/ITQ-2, the Ni/ITQ-2-co sample prepared by

using Ni-cyclen as the precursor for impregnation showed a markedly higher rate (168 g_{SA} g_{Ni}^{-1} h^{-1}), which was consistent with the relative average sizes of the Ni nanoparticles. Despite the comparable Ni loadings in the two 2D samples, the smaller sizes and higher dispersion of the Ni nanoparticles in Ni/ITQ-2-co provided more metal active sites for the deoxygenation of SA than Ni/ITQ-2. The large external surface area, highly dispersed Ni nanoparticles, and abundant accessible active sites on Ni/ITQ-2-co reduced the diffusion limitation, provided more active sites and showed superior activity in the deoxygenation reaction of SA compared to most reported catalysts (Table S2).

The conversion of SA and the product distributions on Ni/ITQ-2 and Ni/ITQ-2-co are shown in Fig. 4b, c. After reacting for 4 h, the Ni/ITQ-2-co catalyst afforded 98% conversion of the SA, which was much higher than that seen with Ni/ITQ-2 (70%). The main products for both catalysts were n-octadecane (n-C_{18}) and n-heptadecane (n-C_{17}), suggesting that decarboxylation/decarbonylation occurred in addition to hydrodeoxygenation of the SA[11]. It is worth noting that the ratios of n-C_{18} to n-C_{17} (~2.5 in molar) were comparable for Ni/ITQ-2 and Ni/ITQ-2-co, indicating that the SA deoxygenation reactions on Ni/ITQ-2 and Ni/ITQ-2-co used the same pathway. Thus, the excellent catalytic performance of Ni/ITQ-2-co was attributed to highly dispersed Ni nanoparticles immobilized on ITQ-2 via the ligand-chelating impregnation approach. To expand the substrate scope, the deoxygenation of palm oil, which is rich in hexadecanoic and octadecanoic acids, was carried out over Ni/ITQ-2-co. As shown in Fig. 4d, the main products were n-C_{15}–C_{18} alkanes, and the yield of diesel-range alkanes was 83 wt%, which was close to the theoretical yield of 85 wt%.

After the reactions, the Ni/ITQ-2 and Ni/ITQ-2-co were collected by centrifugation, washed with acetone, and dried overnight for regeneration. The activity of the Ni/ITQ-2-co catalyst was nearly unchanged after four consecutive cycles (57% to 53%, as shown in Fig. 4e), whereas the efficiency for conversion of SA over Ni/ITQ-2 was decreased to half of the initial efficiency after four cycles (Fig. 4f). To explain the different stabilities, the Ni loadings of both catalysts were measured via ICP−OES. The results showed slight decreases in the Ni loadings on Ni/ITQ-2 (2.33 wt%) and Ni/ITQ-2-co (2.51 wt%) after the reaction (Table S1). This indicated that the 2D support with abundant defect sites and high external surface area facilitated immobilization of the Ni clusters during the reaction. Furthermore, a TEM analysis was performed on the used Ni/ITQ-2 and Ni/ITQ-2-co to determine the sizes of the Ni nanoparticles after the reactions. As shown in Fig. S8, obvious aggregation of the Ni clusters had occurred for Ni/ITQ-2 after the deoxygenation reaction of SA, which resulted in a significant increase in the average
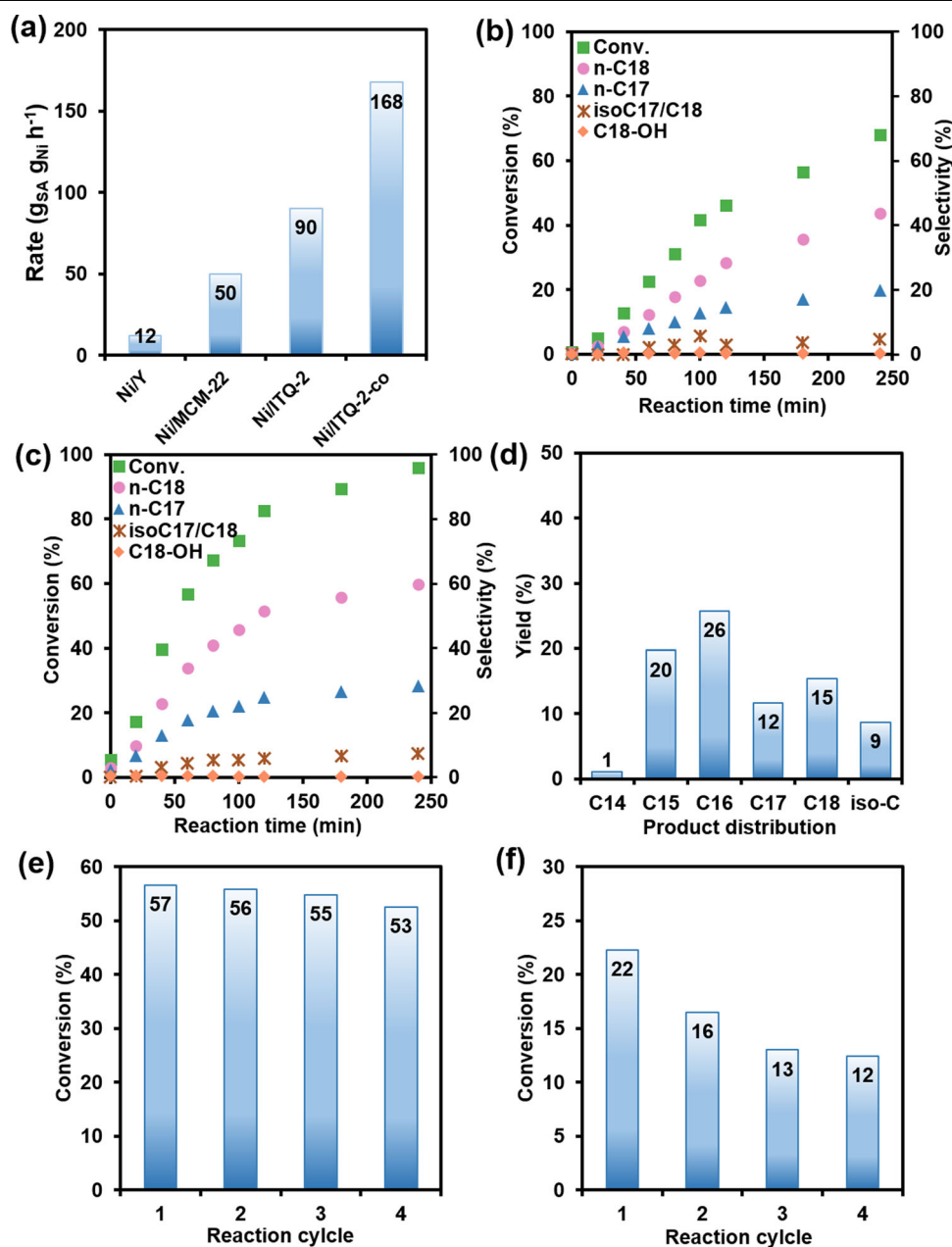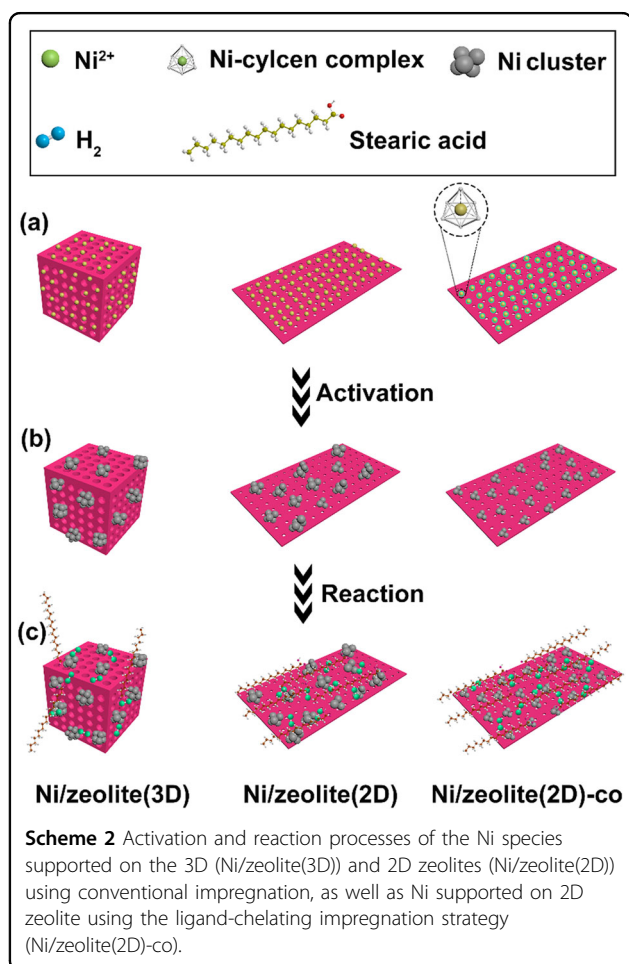
Fig. 4 Catalytic performance of prepared Ni/zeolite catalysts for deoxygenation reactions of SA. Comparison of normalized rates for SA conversion over the prepared Ni/zeolites (**a**); Time-dependent conversions of SA and product selectivities seen with Ni/ITQ-2 (**b**) and Ni/ITQ-2-co (**c**). Product compositions after the deoxygenation of palm oil over Ni/ITQ-2-co (**d**). Reaction conditions: 260 °C, 4 MPa H_2, time = 4 h. stirring speed = 1000 rpm, stearic acid/catalyst = 10 by mass. The conversion of SA and the selectivity for each product were calculated with Equations S2 and S3. The yield of each product was calculated with Equation S4; recycling tests of Ni/ITQ-2-co (**e**) and Ni/ITQ-2 (**f**) for the deoxygenation reaction of SA. Reaction conditions: 260 °C, 4 MPa H_2, time = 1 h, stirring speed = 1000 rpm, stearic acid/catalyst = 10 by mass.

size of the Ni clusters from 6.4 nm to 17.0 nm. In contrast, the average size of the Ni nanoparticles on Ni/ITQ-2-co had increased only slightly from 3.8 nm to 5.3 nm after the reaction. Therefore, the excellent stability of Ni/ITQ-2-co was attributed to the stable Ni sites that resulted from the strong interactions with the ITQ-2 support, as indicated

by the XPS analysis discussed above. The uniform distribution and strong immobilization of Ni on the Ni/ITQ-2-co catalyst effectively suppressed migration of the Ni nanoclusters during the reaction and regeneration processes. Taken together, these findings provide further support for the use of the ligand-chelating impregnation

Scheme 2 Activation and reaction processes of the Ni species supported on the 3D (Ni/zeolite(3D)) and 2D zeolites (Ni/zeolite(2D)) using conventional impregnation, as well as Ni supported on 2D zeolite using the ligand-chelating impregnation strategy (Ni/zeolite(2D)-co).

approach in preparing the Ni/ITQ-2-co catalyst. As illustrated in Scheme 2, the 2D zeolite support facilitated distribution of the Ni species after impregnation, since its external surface area was larger than that of the 3D support (Scheme 2a). During the activation process, the cyclen-chelated Ni complexes underwent stepwise decomposition, unlike the bare Ni^{2+} ions. This process suppressed rapid aggregation of the Ni species and formed highly dispersed Ni nanoclusters on the ITQ-2 zeolite (Scheme 2b). The ligand-chelating impregnation strategy stabilized the highly dispersed Ni nanoclusters on the ITQ-2 zeolite, and this involved protection of the Ni^{2+} by the chelating ligand and immobilization on the 2D zeolite. Consequently, the ITQ-2-supported Ni nanoclusters displayed superior activity and stability during the conversions of palm oil or SA to diesel-range alkanes (Scheme 2c).

Conclusion

In conclusion, a series of 2D and 3D Ni/zeolites was prepared via an impregnation approach and used in sustainable production of diesel fuel via deoxygenation. The present work highlighted the advantages of utilizing a 2D zeolite support with a large external surface area and abundant defect sites, which were beneficial in dispersing the Ni nanoparticles formed via the facile impregnation method. Compared to conventional 3D and laminar zeolite supports, the 2D ITQ-2 zeolite-supported Ni materials exhibited markedly smaller Ni particle sizes and improved transport efficiencies for bulky reactants. Importantly, the ligand-chelated Ni complex used as the precursor for the impregnation process provided smaller Ni nanoparticles and facilitated dispersion via a combination of ligand protection and strong interactions between the Ni species and the 2D ITQ-2 zeolite. Consequently, the Ni/ITQ-2-co catalyst prepared by the ligand-chelating impregnation approach showed superior activity and stability in the deoxygenation reactions of SA or palm oil, and this offers a promising solution for renewable production of diesel fuel.

Author details
[1]State Key Laboratory of Inorganic Synthesis and Preparative Chemistry, College of Chemistry, Jilin University, 2699 Qianjin Street, Changchun 130012, P. R. China. [2]International Center of Future Science, Jilin University, 2699 Qianjin Street, Changchun 130012, P. R. China. [3]Electron Microscopy Center, Jilin University, 2699 Qianjin Street, Changchun 130012, P. R. China

Author contributions
J.Y. and G.Y. designed the experiments and prepared the manuscript. H.P. and G.Y. conducted the syntheses, characterizations, and catalyst evaluations. All authors discussed the results and commented on the manuscript.

Competing interests
The authors declare no competing interests.

Publisher's note
Springer Nature remains neutral with regard to jurisdictional claims in published maps and institutional affiliations.

References
1. Yusuf, N. N. A. N., Kamarudin, S. K. & Yaakub, Z. Overview on the current trends in biodiesel production. *Energy Convers. Manag.* **52**, 2741–2751 (2011).
2. Pang, H., Yang, G., Li, L. & Yu, J. Efficient transesterification over two-dimensional zeolites for sustainable biodiesel production. *Green. Energy Environ.* **5**, 405–413 (2020).
3. Amini, Z., Ilham, Z., Ong, H. C., Mazaheri, H. & Chen, W.-H. State of the art and prospective of lipase-catalyzed transesterification reaction for biodiesel production. *Energy Convers. Manag.* **141**, 339–353 (2017).
4. Demirbas, A. Comparison of transesterification methods for production of biodiesel from vegetable oils and fats. *Energy Convers. Manag.* **49**, 125–130 (2008).

5. Demirbas, A. Progress and recent trends in biodiesel fuels. *Energy Convers. Manag.* **50**, 14–34 (2009).

6. Ma, B., Cui, H. M., Wang, D. R., Wu, P. & Zhao, C. Controllable hydrothermal synthesis of Ni/H-BEA with a hierarchical core-shell structure and highly enhanced biomass hydrodeoxygenation performance. *Nanoscale* **9**, 5986–5995 (2017).

7. Ma, B., Yi, X. F., Chen, L., Zheng, A. M. & Zhao, C. Interconnected hierarchical HUSY zeolite-loaded Ni nano-particles probed for hydrodeoxygenation of fatty acids, fatty esters, and palm oil. *J. Mater. Chem. A* **4**, 11330–11341 (2016).

8. Foraita, S. et al. Controlling hydrodeoxygenation of stearic acid to n-Heptadecane and n-Octadecane by adjusting the chemical properties of Ni/SiO$_2$-ZrO$_2$ catalyst. *Chemcatchem* **9**, 195–203 (2017).

9. Kubička, D. & Kaluža, L. Deoxygenation of vegetable oils over sulfided Ni, Mo and NiMo catalysts. *Appl. Catal. A* **372**, 199–208 (2010).

10. Kubičková, I., Snåre, M., Eränen, K., Mäki-Arvela, P. & Murzin, D. Y. Hydrocarbons for diesel fuel via decarboxylation of vegetable oils. *Catal. Today* **106**, 197–200 (2005).

11. Di, L. et al. Robust ruthenium catalysts for the selective conversion of stearic acid to diesel-range alkanes. *Appl. Catal. B* **201**, 137–149 (2017).

12. Janampelli, S. & Darbha, S. Selective and reusable Pt-WO$_x$/Al$_2$O$_3$ catalyst for deoxygenation of fatty acids and their esters to diesel-range hydrocarbons. *Catal. Today* **309**, 219–226 (2018).

13. Hengsawad, T., Jindarat, T., Resasco, D. E. & Jongpatiwut, S. Synergistic effect of oxygen vacancies and highly dispersed Pd nanoparticles over Pd-loaded TiO$_2$ prepared by a single-step sol–gel process for deoxygenation of triglycerides. *Appl. Catal. A* **566**, 74–86 (2018).

14. Cheah, K. W. et al. Monometallic and bimetallic catalysts based on Pd, Cu and Ni for hydrogen transfer deoxygenation of a prototypical fatty acid to diesel range hydrocarbons. *Catal. Today* **355**, 882–892 (2020).

15. Kamaruzaman, M. F., Taufiq-Yap, Y. H. & Derawi, D. Green diesel production from palm fatty acid distillate over SBA-15-supported nickel, cobalt, and nickel/cobalt catalysts. *Biomass-. Bioenergy* **134**, 105476 (2020).

16. Song, W. J., Liu, Y. S., Barath, E., Zhao, C. & Lercher, J. A. Synergistic effects of Ni and acid sites for hydrogenation and C-O bond cleavage of substituted phenols. *Green. Chem.* **17**, 1204–1218 (2015).

17. Liu, S. et al. Cascade adsorptive separation of light hydrocarbons by commercial zeolites. *J. Energy Chem.* **72**, 299–305 (2022).

18. Di, J., Li, L., Wang, Q. & Yu, J. Porous membranes with special wettabilities: designed fabrication and emerging application. *CCS Chem.* **3**, 2280–2297 (2021).

19. Chai, Y., Dai, W., Wu, G., Guan, N. & Li, L. Confinement in a zeolite and zeolite catalysis. *Acc. Chem. Res.* **54**, 2894–2904 (2021).

20. Yu, J. & Zhao, D. Preface to special topic on new era of zeolite science. *Natl Sci. Rev.* **9**, nwac157 (2022).

21. Shi, T. et al. Scalable synthesis of ultrastable lead halide perovskite-zeolite composites via a chemical vapor method in air. *NPG Asia Mater.* **14**, 87 (2022).

22. Sudarsanam, P., Peeters, E., Makshina, E. V., Parvulescu, V. I. & Sels, B. F. Advances in porous and nanoscale catalysts for viable biomass conversion. *Chem. Soc. Rev.* **48**, 2366–2421 (2019).

23. Luo, W. et al. Zeolite-supported metal catalysts for selective hydrodeoxygenation of biomass-derived platform molecules. *Green. Chem.* **21**, 3744–3768 (2019).

24. Shi, Y. et al. Recent progress on upgrading of bio-oil to hydrocarbons over metal/zeolite bifunctional catalysts. *Catal. Sci. Technol.* **7**, 2385–2415 (2017).

25. Wang, N., Sun, Q. & Yu, J. Ultrasmall metal nanoparticles confined within crystalline nanoporous materials: a fascinating class of nanocatalysts. *Adv. Mater.* **31**, 1803966 (2019).

26. Song, W. J., Zhao, C. & Lercher, J. A. Importance of size and distribution of Ni nanoparticles for the hydrodeoxygenation of microalgae oil. *Chem. Eur. J.* **19**, 9833–9842 (2013).

27. Wu, G., Zhang, N., Dai, W., Guan, N. & Li, L. Construction of bifunctional Co/H-ZSM-5 catalysts for the hydrodeoxygenation of stearic acid to diesel-range alkanes. *ChemSusChem* **11**, 2179–2188 (2018).

28. Corma, A., Fornes, V., Pergher, S. B., Maesen, T. L. M. & Buglass, J. G. Delaminated zeolite precursors as selective acidic catalysts. *Nature* **396**, 353 (1998).

29. Oleksiak, M. D. et al. Organic-free synthesis of a highly siliceous Faujasite zeolite with spatially biased Q(4)(nAl) Si speciation. *Angew. Chem. Int. Ed.* **56**, 13366–13371 (2017).

30. Pang, H., Yang, G., Li, L. & Yu, J. Esterification of oleic acid to produce biodiesel over 12-tungstophosphoric acid anchored two-dimensional zeolite. *Chem. Res. Chin. Univ.* **37**, 1072–1078 (2021).

31. Yan, Z. et al. On the acid-dealumination of USY zeolite: a solid state NMR investigation. *J. Mol. Catal. A: Chem.* **194**, 153–167 (2003).

32. Zhang, L., Chen, K., Chen, B., White, J. L. & Resasco, D. E. Factors that determine zeolite stability in hot liquid water. *J. Am. Chem. Soc.* **137**, 11810–11819 (2015).

33. Corma, A. et al. Characterization and catalytic activity of MCM-22 and MCM-56 compared with ITQ-2. *J. Catal.* **191**, 218–224 (2000).

34. Machado, V., Rocha, J., Carvalho, A. P. & Martins, A. Modification of MCM-22 zeolite through sequential post-synthesis treatments. Implications on the acidic and catalytic behaviour. *Appl. Catal. A* **445-446**, 329–338 (2012).

35. Qiu, Z. et al. Tailoring the local environment of silver in SSZ-13 zeolites for low-temperature catalytic oxidation of ammonia. *Appl. Surf. Sci.* **598**, 153856 (2022).

36. Unverricht, S., Hunger, M., Ernst, S., Karge, H. G. & Weitkamp, J. Zeolite MCM-22: synthesis, dealumination and structural characterization. *Stud. Surf. Sci. Catal.* **84**, 37–44 (1994).

37. Shu, Y., Ma, D., Xu, L., Xu, Y. & Bao, X. Methane dehydro-aromatization over Mo/MCM-22 catalysts: a highly selective catalyst for the formation of benzene. *Catal. Lett.* **70**, 67–73 (2000).

38. Chen, B.-H. et al. Towards a full understanding of the nature of Ni(ii) species and hydroxyl groups over highly siliceous HZSM-5 zeolite supported nickel catalysts prepared by a deposition–precipitation method. *Dalton T* **45**, 2720–2739 (2016).

39. Bacariza, M. C., Amjad, S., Teixeira, P., Lopes, J. M. & Henriques, C. Boosting Ni dispersion on zeolite-supported catalysts for CO$_2$ methanation: the influence of the impregnation solvent. *Energy Fuels* **34**, 14656–14666 (2020).

40. Bacariza, M. C. et al. CO$_2$ hydrogenation over Ni-based zeolites: effect of catalysts preparation and pre-reduction conditions on methanation performance. *Top. Catal.* **59**, 314–325 (2016).

41. Zanjanchi, M. A. & Razavi, A. Identification and estimation of extra-framework aluminium in acidic mazzite by diffuse reflectance spectroscopy. *Spectrochim. Acta, Part A* **57**, 119–127 (2001).

42. Espinosa-Alonso, L., de Jong, K. P. & Weckhuysen, B. M. Effect of the Nickel precursor on the impregnation and drying of γ-Al$_2$O$_3$ catalyst bodies: A UV—vis and IR microspectroscopic study. *J. Phys. Chem. C.* **112**, 7201–7209 (2008).

43. Hass, E. C. & Plath, P. J. UV-visible transmission microscope spectrophotometry on x-type zeolites: Part I. Formation of different nickel complexes in zeolite X. *J. Mol. Catal.* **14**, 35–52 (1982).

44. Négrier, F. et al. A systematic study of the interactions between chemical partners (metal, ligands, counterions, and support) involved in the design of Al$_2$O$_3$-supported nickel catalysts from Diamine—Ni(II) Chelates. *J. Phys. Chem. B* **109**, 2836–2845 (2005).

45. Sun, K.-Q., Marceau, E. & Che, M. Evolution of nickel speciation during preparation of Ni–SiO$_2$ catalysts: effect of the number of chelating ligands in [Ni(en)$_x$(H$_2$O)$_{6-2x}$]$^{2+}$ precursor complexes. *Phys. Chem. Chem. Phys.* **8**, 1731–1738 (2006).

46. Qi, Y., Qi, H., Li, J. & Lu, C. Synthesis, microstructures and UV–vis absorption properties of β-Ni(OH)$_2$ nanoplates and NiO nanostructures. *J. Cryst. Growth* **310**, 4221–4225 (2008).

47. Bacariza, M. C., Maleval, M., Graça, I., Lopes, J. M. & Henriques, C. Power-to-methane over Ni/zeolites: Influence of the framework type. *Microporous Mesoporous Mater.* **274**, 102–112 (2019).

48. Zahmakıran, M. et al. Zeolite framework stabilized nickel(0) nanoparticles: active and long-lived catalyst for hydrogen generation from the hydrolysis of ammonia-borane and sodium borohydride. *Catal. Today* **170**, 76–84 (2011).

49. Kumari, S. & Ray, S. Zeolite encapsulated Ni(ii) Schiff-base complexes: improved catalysis and site isolation. *N. J. Chem.* **44**, 14953–14963 (2020).

50. Guczi, L. & Bazin, D. Structure and selectivity of metal catalysts: revisiting bimetallic zeolite systems. *Appl. Catal. A* **188**, 163–174 (1999).

51. Fukuoka, A. et al. Preparation, XAFS characterization, and catalysis of platinum nanowires and nanoparticles in mesoporous silica FSM-16. *Top. Catal.* **18**, 73–78 (2002).